

**Ultrafast demagnetization of FePt:Cu thin films and the role of magnetic heat capacity**Johannes Kimling,<sup>1,\*</sup> Judith Kimling,<sup>1</sup> R. B. Wilson,<sup>1</sup> Birgit Hebler,<sup>2</sup> Manfred Albrecht,<sup>2</sup> and David G. Cahill<sup>1</sup><sup>1</sup>*Department of Materials Science and Engineering and Materials Research Laboratory, University of Illinois, Urbana, Illinois 61801, USA*<sup>2</sup>*Institute of Physics, University of Augsburg, Universitätsstrasse 1, 86159 Augsburg, Germany*

(Received 10 September 2014; revised manuscript received 30 October 2014; published 5 December 2014)

The phenomenon of different time scales of ultrafast demagnetization has attracted much attention. This so-called diversity of ultrafast demagnetization has been explained by the microscopic three temperature model (M3TM) and by the Landau-Lifshitz-Bloch model (LLBM). Here, we revisit the basic three temperature model (3TM) and provide a general criterion for explaining the different time scales observed. We focus on the role of magnetic heat capacity, which we find mainly determines the slowing down of the demagnetization time with increasing ambient temperature and laser fluence. In this context, we clarify the role of magnetic heat capacity in the M3TM and compare the 3TM with the LLBM. To illustrate the role of magnetic heat capacity, we present a simulation of ultrafast demagnetization of Ni. Furthermore, we present time-resolved magneto-optic Kerr effect measurements of ultrafast demagnetization and specific heat of Fe<sub>46</sub>Cu<sub>6</sub>Pt<sub>48</sub> from 300 K to close to its Curie temperature. While most of the prior experimental research used high-fluence laser pulses causing sizable temperature excursions of the sample, our experiments involve small temperature excursions, which are crucial for studying the role of magnetic heat capacity in ultrafast demagnetization. Our experimental results corroborate that the slowing down of ultrafast demagnetization is dominated by the increase of the magnetic heat capacity near the Curie temperature.

DOI: [10.1103/PhysRevB.90.224408](https://doi.org/10.1103/PhysRevB.90.224408)

PACS number(s): 75.78.Jp, 75.40.Gb, 75.40.Cx, 75.70.-i

**I. INTRODUCTION**

The field of ultrafast magnetization dynamics is concerned with processes faster than approximately 100 ps [1]. An important problem is the transfer of angular momentum on short time scales, known as ultrafast demagnetization and observed, e.g., in ferromagnetic metals using pump-probe experiments [2]. In their pioneering work, Beaurepaire *et al.* described the time evolution of the magnetization after laser excitation using a phenomenological three temperature model (3TM) that considers energy exchange between three thermodynamic reservoirs (electrons, phonons, and magnetization) [3]. Thereafter, the problem of magnetization dynamics at fs-time scales was addressed by the theoretical study of Hübner *et al.* [4]. To date, the number of competing theories of ultrafast demagnetization is still increasing, e.g., in Ref. [5], nine possible mechanisms are summarized. Progress in this field is hampered by the complexity of the theoretical problem and the short time scale that makes experimental tests difficult.

Experiments in the past decade have revealed a “diversity of ultrafast demagnetization” [6], which essentially comprises the following phenomena.

- (i) Sub-ps demagnetization followed by ps remagnetization (e.g., in Ni [3], Co [7], and Fe [8]).
- (ii) Sub-ps demagnetization followed by a second slower demagnetization step that can extend to approximately 100 ps (e.g., in Gd [9] and Tb [10]).
- (iii) Increasing de- and remagnetization time with rising ambient temperature or laser fluence (e.g., in CuCr<sub>2</sub>Se<sub>4</sub> [11], Ni [12], and Gd [13]).
- (iv) Transition from (i) to (ii) at a critical ambient temperature or laser fluence (e.g., in Sr<sub>2</sub>FeMoO<sub>6</sub> [14], Ni [15], and FePt [16]).

Phenomenon (i) has been termed “one-step” or “type I” behavior, while phenomenon (ii) is often referred to as “two-step” or “type II” behavior [6,15]. In the critical regime near the Curie temperature, phenomenon (iii) is also known as “critical slowing down” of magnetization dynamics.

The observation of phenomena (i) through (iv) has been explained by the so-called microscopic three temperature model (M3TM) and by the Landau-Lifshitz-Bloch model (LLBM). The M3TM couples a rate equation for the magnetization to a two-temperature model of phonons and electrons, and includes a spin-flip parameter associated with the Elliot-Yafet theory of spin relaxation [6]. The LLBM is a micromagnetic approach for simulations of a many macrospin system at finite temperature [17,18].

More recently, higher level 3TMs have been developed by Ma *et al.* and by Manchon *et al.* [19,20]. Ma *et al.* use a molecular dynamics approach including thermal coupling between electron, lattice, and magnetization reservoirs via Langevin dynamics [19]. However, they focus on the influence of magnetic and electronic excitations on high strain-rate plastic deformations of magnetic materials, and do not address the “diversity of ultrafast demagnetization” summarized above. The model of Manchon *et al.* employs a self-consistent random phase approximation to solve the Heisenberg Hamiltonian describing the magnetization reservoir [20]. Manchon *et al.* derive an electron-spin relaxation rate that is proportional to the cube of the magnetic-order parameter, and thus becomes vanishingly small near the Curie temperature. Although Manchon *et al.* consider the critical behavior of magnetic heat capacity, they explain phenomena (iii) and (iv) with a reduction of the magnetic order parameter that results in “a weakening of the effective electron-spin interaction (. . .)” [20].

Here, we focus on the role of magnetic heat capacity in ultrafast demagnetization. In Sec. II, we revisit the basic 3TM and provide a simple criterion for explaining the “diversity of ultrafast demagnetization.” To illustrate the role of magnetic heat capacity, we present a simulation of ultrafast

\*kimling@illinois.edu

demagnetization of Ni. In Sec. III, we report experimental results of the temperature dependence of ultrafast demagnetization and specific heat of Fe<sub>46</sub>Cu<sub>6</sub>Pt<sub>48</sub>. In Sec. IV, we discuss the role of magnetic heat capacity in prior research.

## II. THEORY

### A. Three temperature model revisited

The phenomenon of ultrafast demagnetization starts with a short laser pulse, typically of Gaussian shape with a FWHM of 50 fs, exciting electrons to high energies ( $\sim 1$  eV) above the Fermi level. Within approximately 10 fs the excited electrons thermalize via electron-electron interactions and begin transferring excess energy to other thermodynamic reservoirs, e.g., via excitation of phonons, spin waves, and spin fluctuations. The 3TM is based on the assumption of three thermodynamic reservoirs: electrons at temperature  $T_e$ , phonons at temperature  $T_p$ , and magnetization at temperature  $T_s$ . The 3TM considers energy exchange between these reservoirs [3]. We note that computation of magnetic properties of itinerant ferromagnets at finite temperatures, as well as evaluation of the temperature of a dynamic spin system are subjects of current research [21,22]. Since in the ferromagnetic transition metals energy transfer between magnetization and phonons is much smaller than energy transfer between magnetization and electrons [19], we neglect the coupling between magnetization and phonons. In this case, the 3TM in one dimension reads

$$C_e \frac{dT_e}{dt} = g_{ep}(T_p - T_e) + g_{es}(T_s - T_e) + \Lambda_e \frac{d^2 T_e}{dx^2} + P(t), \quad (1)$$

$$C_p \frac{dT_p}{dt} = g_{ep}(T_e - T_p) + \Lambda_p \frac{d^2 T_p}{dx^2}, \quad (2)$$

$$C_s \frac{dT_s}{dt} = g_{es}(T_e - T_s) + \Lambda_s \frac{d^2 T_s}{dx^2}, \quad (3)$$

where  $C$  denotes specific heat,  $g$  denotes energy transfer coefficient,  $\Lambda$  denotes thermal conductivity, and the subscripts e, p, and s refer to the thermodynamic reservoirs of electrons, phonons, and magnetization. The laser energy is transferred to the electron reservoir with a rate  $P(t)$ . As discussed below, heat diffusion into the substrate can influence the remagnetization behavior and the second demagnetization step of phenomenon (ii).

The 3TM is based on the assumption that processes involved in ultrafast demagnetization are slow compared to the internal equilibration time of the respective reservoirs ( $\sim 10$  fs for electrons;  $\sim 1$  ps for phonons and magnetization [1]). Consequently, the 3TM cannot be applied to explain sub-ps demagnetization. At longer time scales, the 3TM describes ultrafast demagnetization via the energy transfer coefficient  $g_{es}$  between electrons and magnetization, without specifying physical mechanisms responsible for ultrafast transfer of angular momentum. The response of the magnetization reservoir is described via the magnetic heat capacity  $C_s$ . According to the theory of critical phenomena, the temperature dependence of magnetization and magnetic heat capacity follow a power law near the Curie temperature [23]. Nanocalorimetric mea-

surements on Ni thin films have shown a broadened peak of the heat capacity at the Curie temperature [24]. Here, we consider the temperature dependence of the magnetic heat capacity  $C_s$  using empirical input as discussed in Sec. III B.

Instantaneously after the onset of the laser pulse heating the electron reservoir, the temperature changes of phonons and spins are still zero. It follows from Eqs. (2) and (3) that the ratio  $R$ , given by

$$R = \frac{g_{es} C_p}{g_{ep} C_s}, \quad (4)$$

determines which temperature,  $T_p$  or  $T_s$ , rises faster. Hence  $R$  provides a general criterion for distinguishing different time scales of ultrafast demagnetization, which does not depend on microscopic parameters. In the limit of small temperature excursions of the phonon and magnetization reservoirs ( $\Delta T/T \ll 1$ ),  $R(t)$  is approximately constant and we find the following criterion.

$R > 1$ .  $T_s$  rises faster than  $T_p$ ; subsequent to the demagnetization process, dominating coupling between electrons and phonons decreases  $T_e$  close to  $T_p < T_s$  resulting in a fast remagnetization until  $T_s = T_p$ . This behavior has been termed “one-step” or “type I” demagnetization [phenomenon (i)].

$R < 1$ .  $T_s$  lags behind  $T_p$ ; subsequent to a fast demagnetization process, dominating coupling between electrons and phonons decreases  $T_e$  close to  $T_p > T_s$  resulting in a second, slower demagnetization step until  $T_s = T_p$ . This behavior has also been called “two-step” or “type II” demagnetization [phenomenon (ii)].

The ratio  $R$  does not depend on the electronic specific heat  $C_e$ , since it characterizes the rise of  $T_s$  with respect to the rise of  $T_p$  providing a case distinction of phenomena (i) and (ii) as well as an explanation for phenomena (iii) and (iv). The electronic specific heat  $C_e$  can influence the sub-ps rise of both  $T_s$  and  $T_p$ . However, if the thermalization time  $\tau_{ep} = C_e/g_{ep}$  of electrons is much shorter than the pulse duration, only a small amount of the energy of the laser pulse is stored in the electron reservoir and the sensitivity of the 3TM to  $C_e$  after the laser pulse is small. If the rise time of the laser pulse is large compared to  $\tau_{ep}$ , the sensitivity of the 3TM to  $C_e$  is small at all times. In both cases,  $R$  describes the ratio of the spin and phonon temperatures at the end of the laser pulse:  $R \approx T_s/T_p$ .

The above case distinction is based on the assumption of a constant  $R(t)$  and does not hold for fluence-dependent measurements that involve sizable temperature excursions of the phonon and magnetization reservoirs ( $\Delta T/T \approx 1$ ) for studying phenomena (iii) and (iv). We note that most prior works used fluence-dependent measurements, which are difficult to analyze due to the unknown temperature dependence of  $R$  [6,15,16,25,26]. Roth *et al.* used both fluence- and temperature-dependent measurements on Ni [15]. However, the temperature-dependent experiments also used a laser fluence of  $3.5 \times 10^{-3} \text{ J cm}^{-2}$ . At 300 K this high fluence resulted in a maximum demagnetization of 58%, which corresponds to a maximum temperature rise of approximately 200 K. Over this temperature interval, the magnetic heat capacity of Ni changes by a factor of approximately 2.6 [27]. Consequently, analysis of high laser fluence experiments results in larger uncertainties compared to low laser fluence experiments.

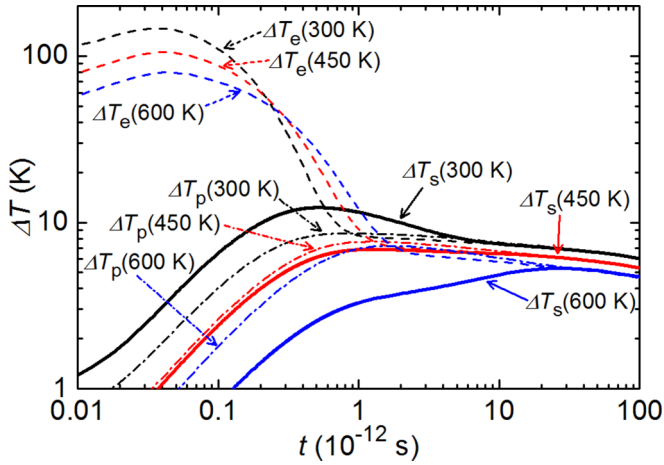


FIG. 1. (Color online) Simulation of the demagnetization behavior of a 15 nm thin Ni layer on a 100 nm SiO<sub>2</sub>/Si substrate using the phenomenological three temperature model. With increasing temperature (black:  $T_0 = 300$  K; red:  $T_0 = 450$  K; blue:  $T_0 = 600$  K) the time evolution of the spin temperature  $\Delta T_s$  (solid lines) changes from a fast demagnetization with subsequent fast remagnetization at 300 K to a slow demagnetization in two steps at 600 K. Also shown are the time evolution of the respective electron and phonon temperatures ( $\Delta T_e$ : dashed lines;  $\Delta T_p$ : dash-dotted lines).

### B. Ultrafast demagnetization of Ni

To illustrate the above case distinction, we apply the 3TM to simulate ultrafast demagnetization of a 15 nm thin Ni layer on a SiO<sub>2</sub>/Si substrate. We consider a Gaussian heat pulse (FWHM = 50 fs centered around  $t = 0$ ) with a fluence of  $42 \times 10^{-6}$  J cm<sup>-2</sup> that results in small temperature excursions of the phonon and magnetization reservoirs ( $\Delta T/T \ll 1$ ). We assume that the absorption profile of the heat pulse decays exponentially in the Ni layer using an optical penetration depth of 15 nm. To account for heat diffusion into the substrate, we extend the 3TM to a multilayer model. The relevant model parameters are summarized in Table I. Since the simulations are performed in the weak perturbation limit, the ratio  $R(t)$  is constant during ultrafast demagnetization. We consider a temperature-dependent energy transfer coefficient

TABLE I. Parameter set for simulation of ultrafast demagnetization of a 15 nm thin Ni layer on a SiO<sub>2</sub>/Si substrate as shown in Fig. 1. [ $T_0$ : ambient temperature;  $C_i$ : volumetric heat capacity of phonons ( $i = p$ ), electrons ( $i = e$ ), and magnetization ( $i = s$ );  $g_{ep}$  and  $g_{es}$ : energy transfer coefficients between electrons and phonons and between electrons and magnetization, respectively;  $R$ : ratio defined in Eq. (4) indicating the demagnetization behavior.]

$T_0$ (K)	$C_p^a$	$C_e^a$ (10 <sup>6</sup> J m <sup>-3</sup> K <sup>-1</sup> )	$C_s^a$	$g_{ep}^b$ (10 <sup>18</sup> W m <sup>-3</sup> K <sup>-1</sup> )	$g_{es}^c$	$R$
300	3.50	0.17	0.20	1.06	0.10	1.65
450	3.64	0.29	0.43	0.94	0.10	0.90
600	3.71	0.42	0.92	0.83	0.10	0.49

<sup>a</sup>Reference [27].

<sup>b</sup>Reference [28].

<sup>c</sup>Free parameter.

between electrons and phonons taken from Ref. [28], and a temperature-dependent electronic heat capacity taken from Ref. [27], although not of importance in our study as discussed above. The only unknown parameter of the model is the energy transfer coefficient  $g_{es}$  between electrons and magnetization. However, for illustrating the above case distinction, it is sufficient to assume a constant  $g_{es} = 1 \times 10^{17}$  W m<sup>-3</sup>K<sup>-1</sup> for every ambient temperature  $T_0$ .

Figure 1 shows the simulated time evolution of  $T_e$  (dashed lines),  $T_p$  (dash-dotted lines), and  $T_s$  (solid lines) after laser excitation at three different ambient temperatures (black:  $T_0 = 300$  K; red:  $T_0 = 450$  K; blue:  $T_0 = 600$  K). The Curie temperature of Ni is  $T_C \approx 633$  [27]. The results cover the “variety of ultrafast demagnetization” described by phenomena (i) through (iv), as predicted by the respective values of  $R$  summarized in Table I. In this simulation, phenomena (iii) and (iv) are caused by the specific heat  $C_s$  of the magnetization, which increases significantly when approaching  $T_C$ . The parameters  $g_{ep}$  and  $C_p$  have a weaker temperature dependence that contributes to a decrease of the demagnetization time — the opposite compared to the effect of  $C_s$ . Hence this simulation demonstrates the significance of the critical behavior of magnetic heat capacity for phenomena (iii) and (iv) in Ni. If  $g_{es}$  decreases with increasing temperature, as predicted in Ref. [20], this will further increase the demagnetization time near the Curie temperature. However, a weakening of the coupling between electron and magnetization is neither required to explain phenomenon (iii) nor phenomenon (iv).

## III. EXPERIMENT

### A. Experimental details

In comparison to Ni, chemically ordered FePt with Cu additions facilitates experiments for studying the relation between ultrafast demagnetization and magnetic heat capacity as a function of temperature due to a perpendicular magnetic anisotropy and a lower Curie temperature. Thin layers of FePt with Cu additions were fabricated using the following approach: a FePt(4.7 nm)/Cu(0.3 nm) bilayer is deposited at room temperature onto 100 nm thick thermal oxide on Si(100) substrates using dc magnetron sputtering (Ar sputter pressure:  $3.5 \times 10^{-3}$  mbar). Rapid thermal annealing (RTA) is employed to transform the bilayer into the L1<sub>0</sub> chemically ordered ternary alloy [29], where the sample is processed for 30 s at 600 °C under N<sub>2</sub> atmosphere (annealing rate: 400 K/s).

The chemical composition of the resulting ternary Fe<sub>46</sub>Cu<sub>6</sub>Pt<sub>48</sub> alloy was determined by Rutherford backscattering spectrometry (RBS). In this study, He<sup>+</sup> ions at an acceleration energy of 1.7 MeV were used. The structural analysis was performed by x-ray diffraction in Bragg-Brentano geometry using Cu  $K\alpha$  radiation, revealing a high degree of chemical L1<sub>0</sub> order with strong (001) texture. Layer thicknesses were determined using x-ray reflectometry.

We use time-resolved measurements of the polar magneto-optic Kerr effect (TR-MOKE) to detect the transient magnetic signal after laser excitation of the 5 nm thin Fe<sub>46</sub>Cu<sub>6</sub>Pt<sub>48</sub> layer. The wavelength of the pump and probe pulses is centered at 783 nm with a FWHM spectral range of  $\sim 10$  nm. Pump and probe pulses are spectrally separated using the two-tint

approach [30]. Instead of the bandpass filter in the incident probe path and the short-pass filter in front of the photodetector used in Ref. [30], we used two ultrasteep short-pass edge filters with a cutoff of 785 nm. Instead of the long-pass filter in the path of the pump beam used in Ref. [30], we used an ultrasteep long-pass edge filter placed in front of the electro-optic modulator. The  $1/e^2$  intensity radius of the focused pump and probe pulses is  $6.1 \mu\text{m}$ ; the FWHM of the convolution of pump and probe pulses is 1.2 ps. The incident probe beam is linearly polarized; the rotation of the polarization on reflection from the surface of the sample is measured by splitting the probe beam with a Wollaston prism and detecting the changes in the intensity of the orthogonal polarization states using a balanced photodetector. The changes in the light intensity convert to the voltage output of the balanced photodetector. We use a double modulation technique with the pump beam modulated at 10.7 MHz using an electro-optic modulator and the probe beam modulated at 200 Hz using a mechanic chopper. Double-modulation suppresses background created by diffusely scattered pump light and coherent pickup by the electronics. We determine the zero time delay using two-photon absorption in a GaP detector.

All measurements were performed using a low incident laser fluence of  $74 \times 10^{-6} \text{ J cm}^{-2}$  that results in small temperature excursions of the sample. Using the transfer matrix method we obtain an absorption of incident photons in the  $\text{Fe}_{46}\text{Cu}_6\text{Pt}_{48}$  layer of 57%. The complex index of refraction of the  $\text{Fe}_{46}\text{Cu}_6\text{Pt}_{48}$  layer was measured via ellipsometry yielding  $\tilde{n} = 3.6 + i4.3$ .

In the weak-perturbation limit, changes in the magneto-optic Kerr signal are proportional to changes in the temperature of the magnetization reservoir:  $\Delta\theta(t) \sim \Delta T_s$ . Therefore, in addition to indicating the time evolution of  $T_s$  during ultrafast demagnetization, TR-MOKE can be used to measure the temperature evolution during heat diffusion into the substrate after equilibration of electrons, phonons, and magnetization. In this case, the 3TM shown in Eqs. (1) through (3) reduces to the one dimensional heat diffusion equation, which enables us to determine the heat capacity of the  $\text{Fe}_{46}\text{Cu}_6\text{Pt}_{48}$  layer. This approach is equivalent to the time-domain thermoreflectance (TDTR) method, which assumes that the thermoreflectance signal is proportional to temperature changes of the sample [31]. Therefore, we analyze TR-MOKE data measured between 100 ps and 4 ns after laser-excitation analogously to TDTR measurements considering a multilayer heat diffusion model. In contrast to standard TDTR measurements, where the heat capacity of the metal layer is assumed to be known and the thermal properties of the substrate are fit parameters, we take the thermal properties of the  $\text{SiO}_2/\text{Si}$  substrate as known and determine the specific heat of the  $\text{Fe}_{46}\text{Cu}_6\text{Pt}_{48}$  layer instead. We note that this 5 nm thin layer is not well suited as a transducer for TDTR, because TDTR requires optically thick transducer layers to prevent temperature-induced changes in the optical properties of the materials underneath that can distort the TDTR signal. TR-MOKE circumvents this problem [32].

The Curie temperature of the sample was determined using static MOKE measurements as a function of temperature yielding  $T_C \approx 502 \text{ K}$  (see Supplemental Material [33]). During all measurements, we applied a magnetic field of approximately

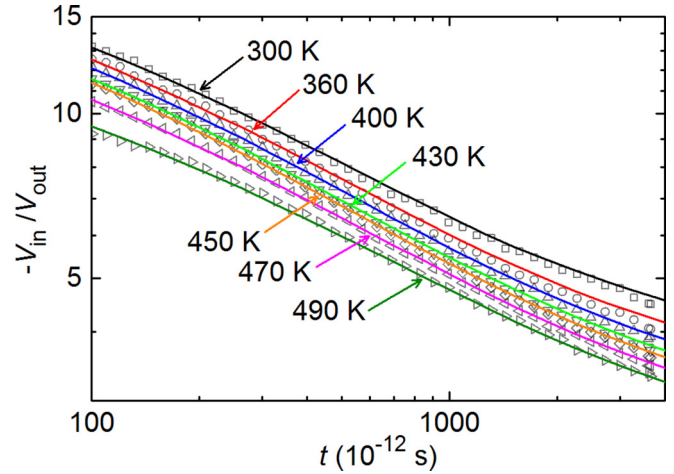


FIG. 2. (Color online) Time evolution of the ratio of the in-phase and out-of-phase components of the TR-MOKE signal,  $-V_{\text{in}}/V_{\text{out}}$  (symbols), measured on a 5 nm thin  $\text{Fe}_{46}\text{Cu}_6\text{Pt}_{48}$  layer on a 100 nm  $\text{SiO}_2/\text{Si}$  substrate. In the time range shown, the measurement data can be analyzed analogously to time-domain thermoreflectance measurements. Fit curves (solid lines) were obtained using a multilayer heat diffusion model considering the total specific heat of the  $\text{Fe}_{46}\text{Cu}_6\text{Pt}_{48}$  layer as fit parameter.

350 mT along the easy axis of the sample magnetization. The temperature of the sample is controlled using a heatable stage.

### B. Magnetic heat capacity of $\text{Fe}_{46}\text{Cu}_6\text{Pt}_{48}$

To determine the total specific heat of the  $\text{Fe}_{46}\text{Cu}_6\text{Pt}_{48}$  layer using the approach described above, we analyze the ratio of the in-phase and out-of-phase components of the TR-MOKE signal ( $V_{\text{in}}/V_{\text{out}}$ ) oscillating at the modulation frequency of the pump beam. In analogy to TDTR, this ratio is independent of laser intensities, sample absorptivity, temperature dependence of the magneto-optic Kerr rotation, and is insensitive to accidental nonconcentric alignment of the pump and probe beams [34,35]. Figure 2 depicts the fit curves (solid lines) to the time evolution of the ratio  $V_{\text{in}}/V_{\text{out}}$  determined from TR-MOKE measurements (symbols) at various ambient temperatures between 300 K and 490 K. The temperature dependence of the resulting total specific heat  $C_{\text{tot}}$  is depicted in Fig. 3 as circles. The error bar indicates a systematic error due to uncertainties in the thicknesses of  $\text{Fe}_{46}\text{Cu}_6\text{Pt}_{48}$  thin film ( $5 \text{ nm} \pm 0.5 \text{ nm}$ ) and  $\text{SiO}_2$  layer ( $106 \text{ nm} \pm 3 \text{ nm}$ ). The dashed line follows a power law that diverges at the Curie temperature indicating the strong increase of  $C_s$  when approaching the Curie temperature. The main contributions to  $C_{\text{tot}}$  arise from excitations in the phonon, electron, and magnetization reservoirs, i.e.,  $C_{\text{tot}} \approx C_p + C_e + C_s$ . The sizable increase of  $C_{\text{tot}}$  when approaching  $T_C$  is dominantly caused by  $C_s$  [36], as illustrated by the shaded areas in Fig. 3.

To use  $C_{\text{tot}}$  as input parameter for the 3TM, we have to define the partitioning of  $C_{\text{tot}}$  into  $C_p$ ,  $C_e$ , and  $C_s$ , which is unknown. We set the specific heat of electrons to  $C_e = 30 \text{ kJ m}^{-3}\text{K}^{-1}$  at 300 K and assume a linear increase with temperature. The same value has been used by Mendil *et al.* in their simulation of ultrafast demagnetization of FePt [16].

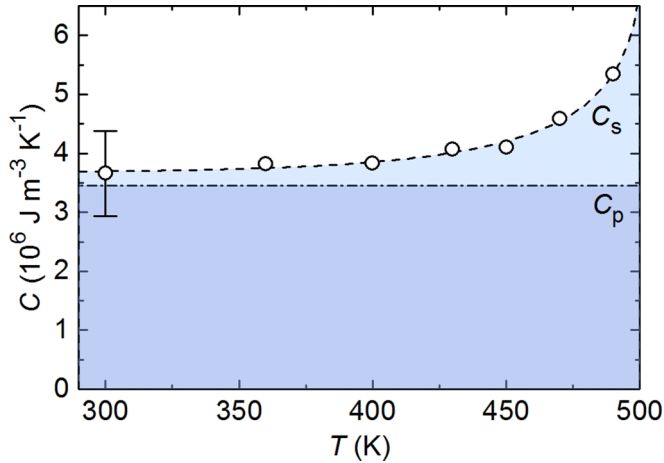


FIG. 3. (Color online) Temperature dependence of the specific heat  $C_{\text{tot}}$  of the 5 nm thin  $\text{Fe}_{46}\text{Cu}_6\text{Pt}_{48}$  layer determined from time-resolved magneto-optic Kerr effect measurements. Dominant contributions to  $C_{\text{tot}}$  arise from phonons ( $C_p$ ) and magnetization ( $C_s$ ). For fitting of the three temperature model to ultrafast demagnetization data we assume a constant  $C_p = 3.46 \times 10^6 \text{ J m}^{-3} \text{ K}^{-1}$  as indicated by the dash-dotted line. The dashed line follows a phenomenological model indicating the strong increase of  $C_s$  when approaching the Curie temperature  $T_C \approx 502 \text{ K}$ . The small electronic specific heat, set to  $C_e = 0.03 \times 10^6 \text{ J m}^{-3} \text{ K}^{-1}$  [16], is not indicated in the diagram.

As an explanation for the small value of  $C_e$ , which is one order of magnitude smaller in comparison to Ni, Mendil *et al.* referred to the reduced density of states at the Fermi energy of FePt. As discussed above, the sensitivity of the 3TM to  $C_e$  is small, if the pulse duration is much longer than the electron thermalization time  $\tau_{\text{ep}} = C_e/g_{\text{ep}}$ . In our experiment,  $\tau_{\text{ep}}$  is of the order of 50 fs, more than one order of magnitude shorter than the pulse duration. Hence accurate knowledge of  $C_e$  is not required. In comparison to  $C_e$ , setting of  $C_p$  is more critical. Due to the large systematic error of  $C_{\text{tot}}$ , independent determination of  $C_p$ , e.g., using the Debye model, would result in a large uncertainty of  $C_s$ . However, as illustrated in Fig. 4, variation of the phononic specific heat from the Dulong-Petit value of  $3.02 \times 10^6 \text{ J m}^{-3} \text{ K}^{-1}$  up to close to  $C_{\text{tot}}(300 \text{ K})$  reveals that the temperature dependence of the fit parameter  $g_{\text{es}}$  is weak above approximately 430 K (shaded area in Fig. 4). This behavior is independent of the choice of  $C_p$ . Since in this temperature range the magnetic heat capacity changes significantly, we conclude that phenomena (iii) and (iv) are governed by the temperature dependence of magnetic heat capacity. A temperature dependence of  $g_{\text{es}}$  below 430 K can result artificially, if  $C_p$  is chosen such that the “base” value  $C_s(300 \text{ K})$  is too small (triangles in Fig. 4) or too large (squares in Fig. 4). Therefore, we set  $C_p = 3.46 \times 10^6 \text{ J m}^{-3} \text{ K}^{-1}$ , such that  $g_{\text{es}}$  shows no clear trend over the whole temperature range.

### C. Ultrafast demagnetization of $\text{Fe}_{46}\text{Cu}_6\text{Pt}_{48}$

To analyze ultrafast demagnetization behavior of  $\text{Fe}_{46}\text{Cu}_6\text{Pt}_{48}$  measured at different temperatures, we match the 3TM to our experiment; i.e., we consider a laser fluence of  $42 \times 10^{-6} \text{ J cm}^{-2}$  with a Gaussian time profile of the convolution of pump and probe pulses (FWHM = 1.2 ps

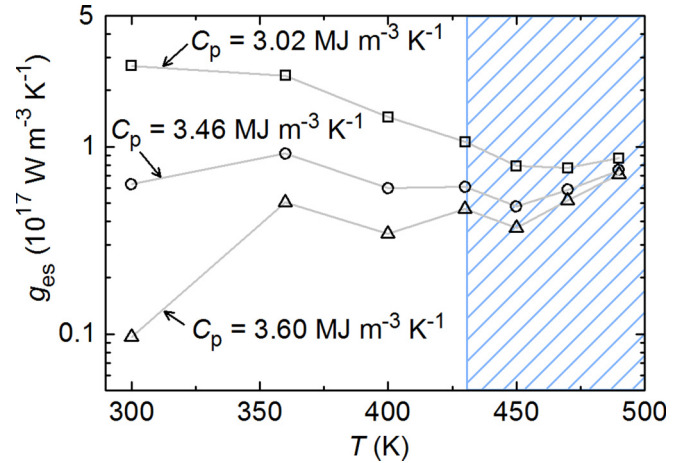


FIG. 4. (Color online) Temperature dependence of the energy transfer coefficient  $g_{\text{es}}$  between electrons and magnetization determined from the three temperature model fitted to ultrafast demagnetization measurements shown in Fig. 5. Depending on the choice of the specific heat  $C_p$  of phonons,  $g_{\text{es}}$  increases (triangles) or decreases (squares) with temperature. However, above  $\sim 430 \text{ K}$  all curves are nearly constant with temperature. In this temperature range, the specific heat  $C_s$  of the magnetization increases significantly governing the demagnetization behavior (compare Fig. 3). Therefore, we set  $C_p = 3.46 \times 10^6 \text{ J m}^{-3} \text{ K}^{-1}$ , such that  $g_{\text{es}}$  is approximately constant with temperature (circles). The resulting fit curves are shown in Fig. 5.

centered around  $t = 0$ ) absorbed in the  $\text{Fe}_{46}\text{Cu}_6\text{Pt}_{48}$  layer assuming an optical penetration depth of 15 nm. To account for heat diffusion into the substrate, we extended the 3TM to a multilayer model. To fit the model to the in-phase component of the measurement signal, we normalize model and measurement data at  $t = 200 \text{ ps}$ . Since the interface thermal conductance between  $\text{Fe}_{46}\text{Cu}_6\text{Pt}_{48}$  layer and the substrate is unknown, we perform the fit in the time range from  $-2 \text{ ps}$  to  $4 \text{ ps}$ . In this time range, the model is insensitive to the interface thermal conductance. The influence of this parameter for  $t > 4 \text{ ps}$  is discussed below. Figure 5 depicts the time evolution of the change in the spin temperature  $T_s$  after laser excitation, determined from TR-MOKE measurements (symbols) at different ambient temperatures indicated in the diagram. Phenomena (i) through (iv) described above are clearly visible in the temperature range investigated. To analyze the measurements within the 3TM, we use the specific heat of the  $\text{Fe}_{46}\text{Cu}_6\text{Pt}_{48}$  layer measured, and assume the partitioning into  $C_p$ ,  $C_e$ , and  $C_s$  as discussed above. The fast remagnetization observed at 300 K depends on the time evolution of the electron temperature that is governed by the energy transfer coefficient  $g_{\text{ep}}$  between electrons and phonons. Therefore, the remaining two free parameters,  $g_{\text{es}}$  and  $g_{\text{ep}}$ , can be determined from a fit of the 3TM to the measurement at 300 K. For the other measurements at higher temperatures, we only consider one free parameter,  $g_{\text{es}}$ , and assume that  $g_{\text{ep}}$  is constant over the temperature range investigated. In this temperature range, for example,  $g_{\text{ep}}$  of Pt is predicted to decrease only by 20% [28]. The parameter set used for the final 3TM simulations is summarized in Table II, together with the ratio  $R$  defined in Eq. (4) indicating that phenomenon

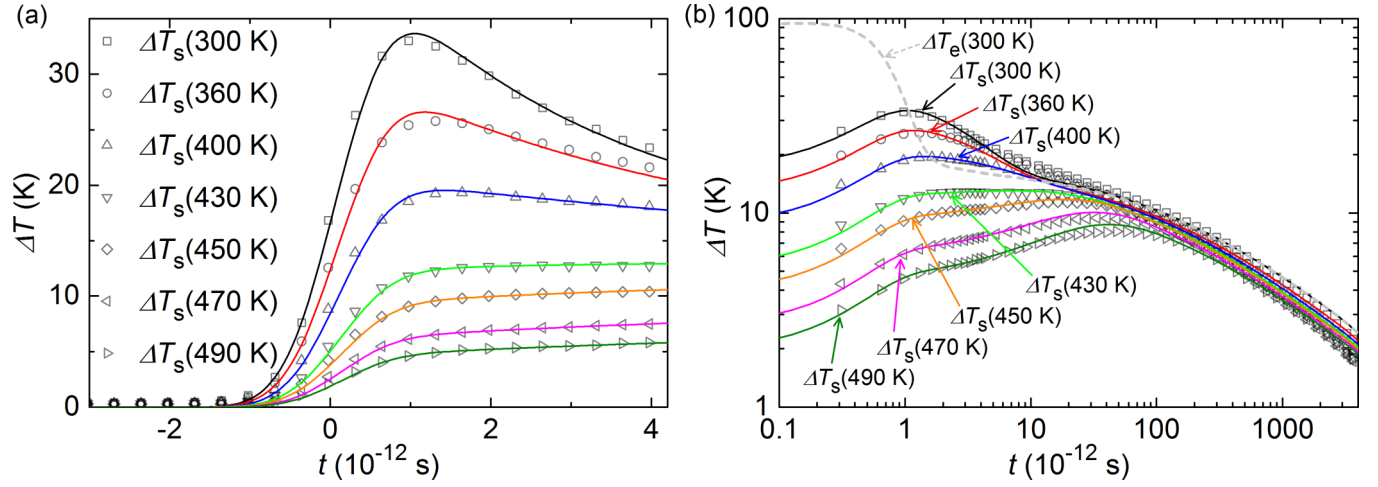


FIG. 5. (Color online) Demagnetization behavior of the 5 nm thin  $\text{Fe}_{46}\text{Cu}_6\text{Pt}_{48}$  layer after low-fluence laser excitation at different ambient temperatures as indicated in the diagrams. Figure (a) shows the time evolution from the onset of the laser pulse up to 4 ps, while (b) shows the time evolution plotted logarithmically from 0.1 ps up to 4 ns including cooling by thermal diffusion. Fit curves (solid lines) to the time-resolved magneto-optic Kerr effect measurements (symbols) were obtained using the phenomenological three temperature model [3TM, Eqs. (1) through (3)] considering the specific heat of the  $\text{Fe}_{46}\text{Cu}_6\text{Pt}_{48}$  layer measured (see caption of Fig. 3). Energy transfer coefficient  $g_{ep}$  was fixed from fitting of the 3TM to the data at ambient temperature  $T_0 = 300$  K. Fit curves to the data at  $T_0 > 300$  K were obtained using one fit parameter,  $g_{es}$ , and assuming constant  $g_{ep}$  in this temperature range. The parameter set is summarized in Table II.

(iv) occurs at approximately 400 K. The fit curves of the 3TM to the measurements are depicted in Fig. 5 as solid lines. Also depicted is the time evolution of the electron temperature  $T_e(300$  K) as dashed line. We emphasize that the only significant change in the dynamics predicted by the 3TM is caused by the change of the magnetic heat capacity. This indicates that phenomena (iii) and (iv) described above are dominated by the temperature dependence of the magnetic heat capacity.

TABLE II. Parameter set of the fit curves shown in Fig. 5. [ $T_0$ : ambient temperature;  $C_i$ : volumetric heat capacity of phonons ( $i = p$ ), electrons ( $i = e$ ), and magnetization ( $i = s$ );  $g_{ep}$  and  $g_{es}$ : energy transfer coefficients between electrons and phonons and between electrons and magnetization, respectively;  $R$ : ratio defined in Eq. (4) indicating the demagnetization behavior.]

$T_0$ (K)	$C_p^a$	$C_e^b$ ( $10^6 \text{ J m}^{-3} \text{ K}^{-1}$ )	$C_s^c$	$g_{ep}^d$ ( $10^{17} \text{ W m}^{-3} \text{ K}^{-1}$ )	$g_{es}^e$	$R$
300	3.46	0.033	0.17	7.00	0.63	1.86
360	3.46	0.040	0.32	7.00	0.92	1.42
400	3.46	0.044	0.33	7.00	0.60	0.91
430	3.46	0.047	0.56	7.00	0.61	0.54
450	3.46	0.050	0.59	7.00	0.48	0.40
470	3.46	0.052	1.08	7.00	0.59	0.27
490	3.46	0.054	1.83	7.00	0.75	0.20

<sup>a</sup>Chosen such that the fit parameter  $g_{es}$  is approximately constant with respect to the temperature. Note that at high temperatures  $g_{es}$  is approximately constant with temperature (see Fig. 4).

<sup>b</sup>Taken from Ref. [16].

<sup>c</sup>Fixed by the constraint  $C_s = C_{\text{tot}} - (C_p + C_e)$ .

<sup>d</sup>Determined from fit to the measurement at  $T_0 = 300$  K. Assumed to be constant for measurements at higher temperatures.

<sup>e</sup>Fit parameter.

The fit curves at 300 K and 360 K show small deviations in the time range between  $\sim 4$  ps and  $\sim 40$  ps (see Fig. 5). These deviations disappear if we assume a finite thermal interface conductance between  $\text{Fe}_{46}\text{Cu}_6\text{Pt}_{48}$  and  $\text{SiO}_2$  (see Supplemental Material [37]). This indicates that the thermal interface conductance can influence the remagnetization process. Since the interface conductance of metals with amorphous materials has hardly been investigated, further research is motivated.

Deviations of the fit curves at large delay times ( $> 1$  ns) originate from changes in the length of the optical path of the pump beam that changes the radius of the pump beam. This error can be minimized using the ratio of the in-phase and out-of-phase components of the measurement signal [34], as shown in Fig. 2.

## IV. DISCUSSION

### A. Role of magnetic heat capacity in prior research

In Ref. [38], Dalla Longa *et al.* derive an analytical solution of the 3TM by neglecting magnetic heat capacity. Although decoupling of Eq. (3) from Eqs. (1) and (2) as done by Dalla Longa *et al.* is justified if the magnetic heat capacity is negligible compared to the electronic heat capacity, this assumption is not typically justified for the problem of ultrafast demagnetization: The temperature of the magnetization reservoir would closely follow the electron temperature and the “diversity of ultrafast demagnetization” described above could not be observed. We assert, counter to the discussion in Ref. [38], that the analytical solution of the 3TM by Dalla Longa *et al.* is based on a different assumption: the energy transfer coefficient  $g_{es}$  between electrons and magnetization is assumed to be much smaller than the energy transfer coefficient  $g_{ep}$  between electrons and phonons.

This misconception about the role of magnetic heat capacity recurred in subsequent research on ultrafast demagnetization

[6,15,39–41]. For example, in the derivation of the M3TM we read the following: “By neglecting the spin specific heat, the electron and phonon dynamics is not affected by the spin system, (...)” [6]. Counter to this, we assert that the M3TM does consider a magnetic heat capacity within the approximations of the mean-field Weiss model. Based on our work, we conclude that the prediction of a critical slowing down [phenomena (iii) and (iv) described above] by the M3TM is based on the critical behavior of the magnetic heat capacity. The authors of Ref. [6] suggest the ratio of Curie temperature and atomic magnetic moment as figure of merit for the demagnetization time of materials with similar spin-flip parameters, without clarifying the role of magnetic heat capacity. Furthermore, this figure of merit does not consider the dynamics of the phonon temperature that is required for describing phenomena (i) through (iv) as discussed in Sec. II A.

The M3TM has been modified by Roth *et al.* to account for magnetic heat capacity (in contrast to the prior M3TM that neglected magnetic heat capacity as discussed by Roth *et al.*) [15]. However, for details on the extended M3TM, the authors refer to a future publication. To explain phenomenon (iv), they state the following: “The reason for such transition is that, close to  $T_C$ , loss of ferromagnetic order results in a weaker exchange splitting  $\Delta_{\text{ex}}$ . Since in the M3TM the rate of demagnetization depends on  $\Delta_{\text{ex}}$  (introduced self-consistently in the model as a function of the magnetization itself), performing the experiments close to  $T_C$  inevitably leads to a slower demagnetization rate” [15]. However, the connection of this explanation with the role of magnetic heat capacity is not discussed by Roth *et al.*

The LLBM explains magnetization dynamics at finite temperatures without the need to define a temperature of the magnetization reservoir. Therefore, the role of magnetic heat capacity in the LLBM as well as the connection of the LLBM and the 3TM have remained unexplored. The LLBM explains the “diversity of ultrafast demagnetization” with two parameters: the coupling to the bath parameter and the longitudinal susceptibility [17,18]. The coupling to the bath parameter describes the coupling strength between electrons and magnetization, while the longitudinal susceptibility accounts for spin fluctuations and dominates the temperature dependence of ultrafast demagnetization. The role of longitudinal susceptibility in the LLBM corresponds to the role of magnetic heat capacity in the 3TM that considers energy fluctuations of the magnetization reservoir. Since these energy fluctuations are determined by spin fluctuations, both LLBM and 3TM can, in principle, predict the same demagnetization behavior as a function of temperature. However, the LLBM is not equivalent to the 3TM. For example, since the LLBM avoids defining a temperature of the magnetization reservoir, the longitudinal susceptibility is evaluated at the temperature  $T_e$  of the electron reservoir, which is assumed as a heat bath. In contrast to that approach, the magnetic heat capacity in the 3TM is evaluated at the temperature  $T_s$  of the magnetization reservoir, which is much lower than  $T_e$  during ultrafast demagnetization. Consequently, the two models (3TM and LLBM) cannot predict the same demagnetization behavior, particularly if either  $T_e$  or  $T_s$  are close to the Curie temperature.

The LLBM has been used, e.g., for analyzing ultrafast demagnetization as a function of temperature in Gd by Sultan *et al.* [13], and as a function of laser fluence in FePt by Mendil *et al.* [16]. Sultan *et al.* state that the observation of phenomenon (iii) in Gd “should provide a key to separate electron- and phonon-mediated spin-flip processes” [13]. Mendil *et al.* “identify that at large pump fluences the resulting electron temperature remains close to  $T_C$  and is leading to critical magnetization fluctuations (...)” [16]. However, the conclusions by Sultan *et al.* and Mendil *et al.* are based on the assumption that spin fluctuations are described correctly by the LLBM. This assumption must be considered with caution, since spin fluctuations are considered at the temperature of the electron reservoir, and described within the approximations of a dynamical mean-field approach.

Characteristic time constants from ultrafast demagnetization experiments are typically determined assuming exponential decay functions [12,14,38,42]. Phenomenon (iii) has been explained qualitatively with critical spin fluctuations, e.g., in half-metallic ferromagnets [14,41], and in transition-metal rare-earth alloys [43]. However, the role of magnetic heat capacity has not been considered for analyzing ultrafast demagnetization as a function of material composition, which might have led to incorrect conclusions. For example, Walowski *et al.* [40] and Radu *et al.* [44], who studied ultrafast demagnetization of permalloy as a function of dopant concentration, explained changes in the demagnetization time in terms of changes in the coupling strength between electrons and magnetization alone. Eschenlohr *et al.*, who studied ultrafast demagnetization of  $\text{Gd}_{1-x}\text{Tb}_x$  alloys as a function of Tb content, did not consider a possible influence from magnetic heat capacity, although in their experiments for high Tb contents the temperature of the magnetization reservoir increases close to the Curie temperature during demagnetization [45].

## B. Role of magnetic heat capacity beyond the weak perturbation limit

Typical experiments on ultrafast demagnetization employ high-fluence lasers with ultrashort pulse durations of approximately 50 fs, which initially generate a highly nonequilibrium state of electrons and finally result in sizable temperature excursions. The 3TM assumes internal thermal equilibrium for each subsystem and does not describe the initial nonequilibrium state during ultrafast demagnetization. It is generally assumed that electrons thermalize with each other within approximately 10 fs, while thermal equilibrium within the magnetization reservoir by excitation and annihilation of spin waves and spin fluctuations is reached within a few picoseconds [1]. Using a model based on the stochastic Landau-Lifshitz-Gilbert equation, Kazantseva *et al.* found that “for spin temperatures above the Curie temperature the system does not necessarily fully demagnetise during the heat pulse” [46]. They conclude that “the spin system is so far from equilibrium that the concept of a spin temperature has to be questioned on the time scale of picoseconds” [46]. However, in contrast to the Landau-Lifshitz-Bloch model, the model of Kazantseva *et al.* does not consider longitudinal spin fluctuations in itinerant ferromagnets. Furthermore, as can be

seen in Fig. 1 of Ref. [46], their model does not predict the experimentally observed two-step demagnetization behavior for high laser fluences [15].

In our experiments we used a low-fluence laser with pulse durations of the order of 1 ps. This enabled us to apply the 3TM and to test our criterion for the demagnetization behavior [Eq. (4)]. However, it is an open question if this criterion and our conclusions on the role of magnetic heat capacity can be generalized for high laser-fluence experiments. We believe that such a generalization is indeed possible, since the initial nonequilibrium state of the magnetization persists only over a short time scale of the order of 1 ps, while the demagnetization process can extend up to several 100 ps for temperatures where magnetic heat capacity significantly determines the magnetization dynamics. Moreover, the demagnetization behavior observed as a function of laser fluence is consistent with predictions from the 3TM; i.e., consideration of the initial nonequilibrium state is not required for explaining the slowing down with increasing laser fluence.

## V. CONCLUSION

In summary, we revisited the basic three temperature model (3TM) of ultrafast demagnetization and provided a general

criterion for explaining the different time scales observed. We clarified the role of magnetic heat capacity in the microscopic three temperature model and compared the 3TM with the Landau-Lifshitz-Bloch model. Furthermore, we presented time-resolved magneto-optic Kerr effect measurements of ultrafast demagnetization and specific heat of  $\text{Fe}_{46}\text{Cu}_6\text{Pt}_{48}$  from 300 K to close to its Curie temperature. In contrast to most of the prior research, our experiments involved small temperature excursions. Our experimental results corroborate that the slowing down of ultrafast demagnetization near the Curie temperature is dominated by the increase in the magnetic heat capacity.

## ACKNOWLEDGMENTS

We thank Gyung-Min Choi and Jun Liu for discussions. This work was carried out in part in the Frederick Seitz Materials Research Laboratory Central Research Facilities, University of Illinois. Financial supports by the Army Research Office under Contract No. W911NF-14-1-0016 and by the German Research Foundation under DFG-Grant No. KI 1893/1-1 and DFG-Grant No. AL 618/21-1 are kindly acknowledged.

- 
- [1] J. Stöhr and H. C. Siegmann, *Magnetism - From Fundamentals to Nanoscale Dynamics* (Springer-Verlag, Berlin, 2006).
  - [2] B. Koopmans, *Handbook of Magnetism and Advanced Magnetic Materials* (John Wiley & Sons, Ltd., New York, 2007), Vol. 3.
  - [3] E. Beaurepaire, J.-C. Merle, A. Daunois, and J.-Y. Bigot, *Phys. Rev. Lett.* **76**, 4250 (1996).
  - [4] W. Hübner and G. P. Zhang, *Phys. Rev. B* **58**, R5920 (1998).
  - [5] C. Illg, M. Haag, and M. Fähnle, *Phys. Rev. B* **88**, 214404 (2013).
  - [6] B. Koopmans, G. Malinowski, F. Dalla Longa, D. Steiauf, M. Fähnle, T. Roth, M. Cinchetti, and M. Aeschlimann, *Nature Mater.* **9**, 259 (2010).
  - [7] J. Güdde, U. Conrad, V. Jähnke, J. Hohlfeld, and E. Matthias, *Phys. Rev. B* **59**, R6608 (1999).
  - [8] T. Kampfrath, R. G. Ulbrich, F. Leuenberger, M. Münzenberg, B. Sass, and W. Felsch, *Phys. Rev. B* **65**, 104429 (2002).
  - [9] A. Melnikov, U. Bovensiepen, I. Radu, O. Krupin, K. Starke, E. Matthias, and M. Wolf, *J. Magn. Magn. Mater.* **272**, 1001 (2004).
  - [10] M. Wietstruk, A. Melnikov, C. Stamm, T. Kachel, N. Pontius, M. Sultan, C. Gahl, M. Weinelt, H. A. Dürr, and U. Bovensiepen, *Phys. Rev. Lett.* **106**, 127401 (2011).
  - [11] T. Ogasawara, K. Ohgushi, Y. Tomioka, K. S. Takahashi, H. Okamoto, M. Kawasaki, and Y. Tokura, *Phys. Rev. Lett.* **94**, 087202 (2005).
  - [12] M. Djordjevic and M. Münzenberg, *Phys. Rev. B* **75**, 012404 (2007).
  - [13] M. Sultan, U. Atxitia, A. Melnikov, O. Chubykalo-Fesenko, and U. Bovensiepen, *Phys. Rev. B* **85**, 184407 (2012).
  - [14] T. Kise, T. Ogasawara, M. Ashida, Y. Tomioka, Y. Tokura, and M. Kuwata-Gonokami, *Phys. Rev. Lett.* **85**, 1986 (2000).
  - [15] T. Roth, A. J. Schellekens, S. Alebrand, O. Schmitt, D. Steil, B. Koopmans, M. Cinchetti, and M. Aeschlimann, *Phys. Rev. X* **2**, 021006 (2012).
  - [16] J. Mendil, P. Nieves, O. Chubykalo-Fesenko, J. Walowski, T. Santos, S. Pisana, and M. Münzenberg, *Sci. Rep.* **4**, 3980 (2014).
  - [17] N. Kazantseva, D. Hinzke, U. Nowak, R. W. Chantrell, U. Atxitia, and O. Chubykalo-Fesenko, *Phys. Rev. B* **77**, 184428 (2008).
  - [18] U. Atxitia and O. Chubykalo-Fesenko, *Phys. Rev. B* **84**, 144414 (2011).
  - [19] P.-W. Ma, S. L. Dudarev, and C. H. Woo, *Phys. Rev. B* **85**, 184301 (2012).
  - [20] A. Manchon, Q. Li, L. Xu, and S. Zhang, *Phys. Rev. B* **85**, 064408 (2012).
  - [21] A. Deák, E. Simon, L. Balogh, L. Szunyogh, M. dos Santos Dias, and J. B. Staunton, *Phys. Rev. B* **89**, 224401 (2014).
  - [22] P.-W. Ma and S. L. Dudarev, *Phys. Rev. B* **86**, 054416 (2012).
  - [23] J. J. Binney, N. J. Dowrick, A. J. Fisher, and M. E. J. Newman, *The Theory of Critical Phenomena* (Oxford University Press, New York, 2002).
  - [24] A. F. Lopeandia, F. Pi, and J. Rodriguez-Viejo, *Appl. Phys. Lett.* **92**, 122503 (2008).
  - [25] U. Atxitia, O. Chubykalo-Fesenko, J. Walowski, A. Mann, and M. Münzenberg, *Phys. Rev. B* **81**, 174401 (2010).
  - [26] B. Y. Mueller, A. Baral, S. Vollmar, M. Cinchetti, M. Aeschlimann, H. C. Schneider, and B. Rethfeld, *Phys. Rev. Lett.* **111**, 167204 (2013).
  - [27] P. J. Meschter, J. W. Wright, C. R. Brooks, and T. G. Kollie, *J. Phys. Chem. Solids* **42**, 861 (1981).
  - [28] Z. Lin, L. V. Zhigilei, and V. Celli, *Phys. Rev. B* **77**, 075133 (2008).

- [29] C. Brombacher, H. Schletter, M. Daniel, P. Matthes, N. Jhrmann, M. Maret, D. Makarov, M. Hietschold, and M. Albrecht, *J. Appl. Phys.* **112**, 073912 (2012).
- [30] K. Kang, Y. K. Koh, C. Chiritescu, X. Zheng, and D. G. Cahill, *Rev. Sci. Instrum.* **79**, 114901 (2008).
- [31] D. G. Cahill, *Rev. Sci. Instrum.* **75**, 5119 (2004).
- [32] J. Liu, G.-M. Choi, and D. G. Cahill (unpublished).
- [33] See Fig. S1 of the Supplemental Material at <http://link.aps.org/supplemental/10.1103/PhysRevB.90.224408> for the static magneto-optic Kerr rotation on reflection from the surface of the sample as function of temperature.
- [34] R. M. Costescu, M. A. Wall, and D. G. Cahill, *Phys. Rev. B* **67**, 054302 (2003).
- [35] J. P. Feser and D. G. Cahill, *Rev. Sci. Instrum.* **83**, 104901 (2012).
- [36] F. Körmann, A. Dick, T. Hickel, and J. Neugebauer, *Phys. Rev. B* **83**, 165114 (2011).
- [37] See Fig. S2 of the Supplemental Material at <http://link.aps.org/supplemental/10.1103/PhysRevB.90.224408> for the influence of a finite interface thermal conductance on the demagnetization behavior.
- [38] F. Dalla Longa, J. T. Kohlhepp, W. J. M. de Jonge, and B. Koopmans, *Phys. Rev. B* **75**, 224431 (2007).
- [39] G. Malinowski, F. Dalla Longa, J. H. H. Rietjens, P. V. Paluskar, R. Huijink, H. J. M. Swagten, and B. Koopmans, *Nat. Phys.* **4**, 855 (2008).
- [40] J. Walowski, G. Müller, M. Djordjevic, M. Münzenberg, M. Kläui, C. A. F. Vaz, and J. A. C. Bland, *Phys. Rev. Lett.* **101**, 237401 (2008).
- [41] G. M. Müller, J. Walowski, M. Djordjevic, G.-X. Miao, A. Gupta, A. V. Ramos, K. Gehrke, V. Moshnyaga, K. Samwer, J. Schmalhorst *et al.*, *Nat. Mater.* **8**, 56 (2009).
- [42] L. Guidoni, E. Beaurepaire, and J.-Y. Bigot, *Phys. Rev. Lett.* **89**, 017401 (2002).
- [43] V. López-Flores, N. Berggaard, V. Halté, C. Stamm, N. Pontius, M. Hehn, E. Otero, E. Beaurepaire, and C. Boeglin, *Phys. Rev. B* **87**, 214412 (2013).
- [44] I. Radu, G. Woltersdorf, M. Kiessling, A. Melnikov, U. Bovensiepen, J.-U. Thiele, and C. H. Back, *Phys. Rev. Lett.* **102**, 117201 (2009).
- [45] A. Eschenlohr, M. Sultan, A. Melnikov, N. Berggaard, J. Wieczorek, T. Kachel, C. Stamm, and U. Bovensiepen, *Phys. Rev. B* **89**, 214423 (2014).
- [46] N. Kazantseva, U. Novak, R. W. Chantrell, J. Hohlfeld, and A. Rebei, *Europhys. Lett.* **81**, 27004 (2008).